

# Quantifying phosphoric acid in high-temperature polymer electrolyte fuel cell components by X-ray tomographic microscopy

S. H. Eberhardt,<sup>a</sup> F. Marone,<sup>b</sup> M. Stampanoni,<sup>b,c</sup> F. N. Büchi<sup>a\*</sup> and T. J. Schmidt<sup>a</sup>

<sup>a</sup>Electrochemistry Laboratory, Paul Scherrer Institut, 5232 Villigen PSI, Switzerland, <sup>b</sup>Swiss Light Source, Paul Scherrer Institut, 5232 Villigen PSI, Switzerland, and <sup>c</sup>Institut für Biomedical Engineering, ETH Zürich, 8092 Zürich, Switzerland. \*E-mail: felix.buechi@psi.ch

Synchrotron-based X-ray tomographic microscopy is investigated for imaging the local distribution and concentration of phosphoric acid in high-temperature polymer electrolyte fuel cells. Phosphoric acid fills the pores of the macro- and microporous fuel cell components. Its concentration in the fuel cell varies over a wide range (40–100 wt% H<sub>3</sub>PO<sub>4</sub>). This renders the quantification and concentration determination challenging. The problem is solved by using propagation-based phase contrast imaging and a referencing method. Fuel cell components with known acid concentrations were used to correlate greyscale values and acid concentrations. Thus calibration curves were established for the gas diffusion layer, catalyst layer and membrane in a non-operating fuel cell. The non-destructive imaging methodology was verified by comparing image-based values for acid content and concentration in the gas diffusion layer with those from chemical analysis.

**Keywords:** high-temperature polymer electrolyte fuel cell (HT-PEFC); X-ray tomographic microscopy; phosphoric acid; concentration.

© 2014 International Union of Crystallography

## 1. Introduction

High-temperature polymer electrolyte membrane fuel cells (HT-PEFCs) are based on phosphoric acid (PA) doped polybenzimidazole (PBI) polymer membranes. With operating temperatures in the range 433–463 K, HT-PEFCs exhibit tolerance to feed gas poisoning of up to 3% CO and at least 10 p.p.m. H<sub>2</sub>S (Schmidt & Baurmeister, 2006) in the anode feed due to decreased adsorption and fast oxidation kinetics at the elevated temperature, respectively. This characteristic renders them especially suitable for stationary combined heat and power (CHP) applications where reformat-based anode feed fuels from, for example, kerosene, natural gas or diesel can be used without complex and expensive gas clean-up. A major requirement for commercialization of PEFCs for the co-generation application is to achieve lifetimes of more than 40000 h without significantly losing performance. Besides degradation of the electrocatalyst, concomitant with deteriorating performance, PA redistribution in the porous components and PA loss by evaporation are the most severe degradation mechanisms limiting the service life of HT-PEFCs. PA discharge rates have been investigated as a function of operating conditions (Yu *et al.*, 2008; Seel *et al.*, 2010); however, no clear understanding of the loss mechanisms and the correlating fuel cell performance has been established yet. The results for acid redistribution from gas diffusion electrode

(GDE) to membrane (Wannek *et al.*, 2009) as well as from membrane electrode assembly (MEA) to porous flow field plates (Hartnig & Schmidt, 2011) highlight the strong mobility of PA and its impact on fuel cell durability. However, the *post mortem* measured data in these studies cannot describe the PA distribution under operation due to diffusion and concentration changes after shutdown and analysis of the fuel cell. A third important aspect is the change of concentration of PA in the MEA as a function of operating parameters. Fuel cell relevant physical properties of the strongly hygroscopic PA electrolyte vary significantly as a function of the local water partial pressure. Consequently, local PA concentration changes during operation. As oxygen diffusivity, viscosity and conductivity (Brown & Whitt, 1952; Korte, 2012) of PA are concentration-dependent, the local concentration changes influence the local electrochemical performance. *In situ* electrochemical impedance spectroscopy (EIS) has shown to be sensitive to changing proton conductivity (Makharia *et al.*, 2005) but no absolute concentration values and only information from the catalyst layer can be extracted.

First *in situ* X-ray imaging measurements on HT-PEFCs have been performed by the ZSW, HZB and Jülich groups (Maier *et al.*, 2010, 2012; Kuhn *et al.*, 2011) using X-ray radiography to investigate the PA distribution and concentration within the membrane, catalyst layer and gas diffusion layer (GDL). The influence of varying current densities on

X-ray transmission changes in the in-plane direction were interpreted as changes in concentration as a result of changes in water partial pressure. However, the simultaneous decrease of concentration and increase in volume, or *vice versa*, prevents the correlation between absorbance and absolute PA concentration. Recently, neutron radiography was also investigated for imaging the PA distribution in HT-PEFC components. It was demonstrated that isotope exchange between  $^1\text{H}$  and  $^2\text{H}$  in PA produces sufficient contrast between PA and the structural components of the HT-PEFC to image the PA distribution (Boillat *et al.*, 2014).

In this work, the characteristics of synchrotron-based X-ray tomographic microscopy (XTM) are investigated when applied for imaging the *distribution* of PA in the membrane electrode assembly of HT-PEFC. All images in the present work are acquired with non-operated components at room temperature. However, the final goal will be to apply this methodology *in operando* at elevated temperatures, similarly as XTM is successfully applied to visualize the water distribution in low-temperature PEFCs (Eller *et al.*, 2011; Flückiger *et al.*, 2011; Krüger *et al.*, 2011). For HT-PEFC, however, there is an additional difficulty, *viz.* the determination of the local PA concentration. For this task a calibration method correlating the local greyscale value of the PA intermixed with the different porous fuel cell components to PA concentration is developed and presented in this communication.

## 2. Materials and methods

### 2.1. Membrane electrode assembly

The HT-PEFC MEA has a sandwich-like structure. The PA-doped PBI membrane is clamped between two GDLs, including a microporous layer (MPL) and the catalyst layer (CL). A schematic representation is shown in Fig. 1. At the anode, hydrogen is oxidized on the electrocatalyst and protons migrate through the proton-conducting membrane to the cathode. In the membrane, the PBI polymer provides a matrix

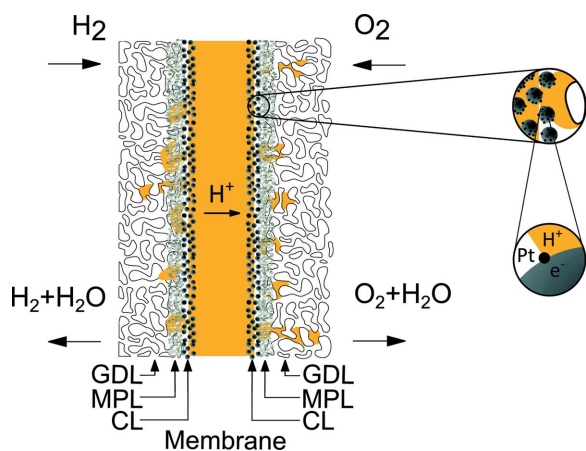


**Figure 1**  
Schematic representation of a HT-PEFC membrane electrode assembly with GDL, MPL, CL, membrane and PA patches in the GDL and MPL (yellow).

for the proton-conducting PA electrolyte. Proton conductivity is defined by the concentration of the acid (Wydeven, 1959; Chin & Chang, 1989) and the PBI/PA ratio (Pahari *et al.*, 2012). On the cathode side, oxygen is reduced to water at the platinum catalyst nanoparticles. Due to the high temperatures, water is formed in vapour form, which directly influences the PA concentration and consequently its physical properties, such as oxygen diffusivity, viscosity, PA vapour pressure and conductivity (Brown & Whitt, 1952; Korte, 2012).

Generally the GDL materials are porous structures with a thickness of 150–300  $\mu\text{m}$  composed of carbon fibres and a carbonaceous binder. The average pore size is of the order of 20–50  $\mu\text{m}$ . For these pores we use the term ‘macropores’ in this communication. The GDL is coated with a so-called MPL (typical pore size of hundreds of nanometres) which in turn is coated by the CL containing the carbon-supported electrocatalyst (similar pore size as the MPL).

The main purpose of the GDL is to provide for electrical conductivity from the CL to the flow field as well as reactant/product gas transport in the void and heat transport in the solid phase. During initial compression of the components, PA is pushed from the membrane through the MPL and GDL, partially filling the empty macro- and micropores of the GDL/MPL and wetting the carbon fibres. The CL is composed of four components: platinum nanoparticles of a few nanometres diameter are supported on carbon black agglomerates, aggregated with a polymeric binder and PA which partially fills the pores.

### 2.2. Sample preparation

For all experiments, BASF Celtec<sup>®</sup> MEAs were used. In these MEAs, the PBI membrane is doped with approximately 25  $\text{mg cm}^{-2}$  of PA and sandwiched between two carbon paper GDLs [proprietary material from SGL carbon (SGL 38) consisting of carbon fibres and a significant volume fraction of microporous binder (pore diameter typically 0.5–5  $\mu\text{m}$ )]. As electrocatalyst, Pt/Vulcan XC-72 (1  $\text{mg}_{\text{Pt}} \text{cm}^{-2}$  on both anode and cathode side) is used. Circular MEA samples of 0.2  $\text{cm}^2$  (diameter 5 mm) were punched out of the larger MEA samples. For the greyscale calibration experiments, these small samples were immersed in glass flasks filled with 5 ml of 40, 60 and 85 wt%  $\text{H}_3\text{PO}_4$  for three weeks, in order to establish equilibrium between PA in the MEA and the solution. Due to the large excess of PA in the vessel, the concentration does not change significantly during equilibration. The MEAs were removed from the glass flasks, assembled in the cell (see below) and imaged within less than 15 min to exclude a significant change in concentration due to the relative humidity of the ambient atmosphere. For the 100 wt% sample, extensive swelling of the membrane occurred resulting in an over-compression of the MEA upon cell assembly and subsequent destruction of the CL and membrane. Therefore, no calibration data for these two components could be deduced. The macroporous GDL, however, was not affected and could be used for evaluation. All tomograms were recorded at a temperature of 293 K. For imaging the porosity

of the PA-free GDL, the sample holder was flushed with 15 ml of deionized water, heated to 373 K and purged with dry nitrogen for 5 min.

The change in grey levels of pure PA with phase and absorption contrast was measured by filling 1 mm-diameter bore holes in a kapton sample holder with 40 wt% and 85 wt% H<sub>3</sub>PO<sub>4</sub>.

### 2.3. PA determination

PA mass of the samples was determined by leaching the samples in defined volumes of pure water and determining the resulting acid concentration in the solution by ion chromatography (IC) using a Metrohm 882 Compact IC Plus equipped with a Metrosepp A Supp 5 150/4.0 anion column. When separating the GDL and MPL/CL, small parts of the MPL were still attached to the GDL resulting in errors for PA mass determination in the GDL. The error is difficult to quantify due to the inhomogeneous distribution of MPL within the GDL and unknown PA mass in the MPL.

### 2.4. X-ray imaging

X-ray tomographic microscopy imaging was performed at the TOMCAT (TOMographic Microscopy and Coherent rAdiology experimenTs) beamline at the Swiss Light Source (Stampanoni *et al.*, 2006). For acquisition of the tomographic scans a specially designed cell (Roth *et al.*, 2013) was used with a circular MEA size of 0.2 cm<sup>2</sup>. All images presented here were recorded in non-operated cells at room temperature. This mode is termed *ex situ*. A total of 2001 projections were acquired during 180° sample rotation (0.09° step angle). For absorption contrast, the sample was positioned as close as possible to the scintillator (10 mm) and projections were reconstructed using an efficient algorithm based on a Fourier method (Marone & Stampanoni, 2012). In contrast, for projections obtained when the sample was located farther away from the scintillator (25 mm), phase retrieval (Paganin *et al.*, 2002) was performed prior to tomographic reconstruction with the above-mentioned algorithm. For phase retrieval,  $\delta$  ( $8.96 \times 10^{-7}$ ) and  $\beta$  ( $1.76 \times 10^{-9}$ ) of the complex index of refraction for 85 wt% PA at 298 K and 20 keV were chosen as input parameters. The sCMOS camera (PCO.edge) had a chip size of 2560 × 2160 pixels. The important imaging parameters are summarized in Table 1. All tomograms were flat- and dark-field corrected. The reconstructed slices were saved in 16-bit TIFF format using constant minimum and maximum grey-level scaling values for all scans. The final tomograms were subsequently normalized by dividing the greyscale values with the maximum value of 65535.

### 2.5. Image calibration

The result of X-ray tomographic imaging (XTM) is greyscale images in which different phases and materials are represented by different greyscale values. If the materials properties of the examined system are known, it is usually

**Table 1**

Imaging parameters for absorption and phase contrast.

Reconstruction algorithm	Distance to detector (mm)	Energy (keV)	Exposure time (ms)	No. exposures per scan	Resulting voxel size (μm)
Absorption	10	20	20	2001	2.2
Phase	25	20	15	2001	2.13

possible to attribute a greyscale value to a specific material in order to determine its spatial distribution. With absorption-contrast-based reconstruction of the tomographic images, the linear relation of greyscale value to linear attenuation coefficient  $\mu$  (cm<sup>-1</sup>) can be used to determine unknown PA concentrations by inter/extrapolation from only two values of known concentration. In the case of the in-line phase contrast, this quantitative relation does not hold, which therefore requires a calibration curve where the greyscale values of a range of concentrations is determined.

In the fuel cell a mixture of PA and carbonaceous binder, carbon fibres and platinum catalyst is present in the GDL and CL. This makes it necessary to establish a referencing/calibration method where the grey levels of mixtures of PA with known concentration with the other materials is determined. Thus a correlation between the greyscale value in the tomographic image and the PA concentration within the MEA components can be established.

## 3. Results and discussion

### 3.1. Evaluation of absorption and phase contrast

With regard to image reconstruction, a reconstruction algorithm has to be chosen which produces best contrast for visualization and quantification of PA within the different porous fuel cell components. Therefore, phase- and absorption-contrast-based techniques were compared by imaging small volumes of pure 40 and 85 wt% H<sub>3</sub>PO<sub>4</sub> in a kapton sample holder. The resulting histograms (distributions of greyscale value of pixels) are shown in Fig. 2. It becomes obvious that phase contrast imaging results in significantly less noise, due to the low pass filtering characteristics of the phase retrieval step (Paganin *et al.*, 2002), resulting in clearly distinctive peaks. Evaluating the peak-to-peak (contrast) distance of 40 and 85 wt% H<sub>3</sub>PO<sub>4</sub> for absorption and phase contrast results in a greyscale difference of 0.064 and 0.095, respectively, indicating an advantage for phase contrast. By tuning the maximum greyscale level for absorption, a slight increase in contrast is expected, while phase contrast could be optimized by tuning the sample-to-detector distance and lowering the greyscale window. Eventually phase-contrast-based reconstruction is chosen due to the increased contrast for the given imaging parameters but most importantly due to the well distinguishable histogram peaks. This is especially important considering that the fuel cell MEA consists of several components of similar greyscale such as, for example, microporous binder and macropores in the GDL both completely or partially filled with PA. Being able to distinguish between these components in terms of histogram peaks makes

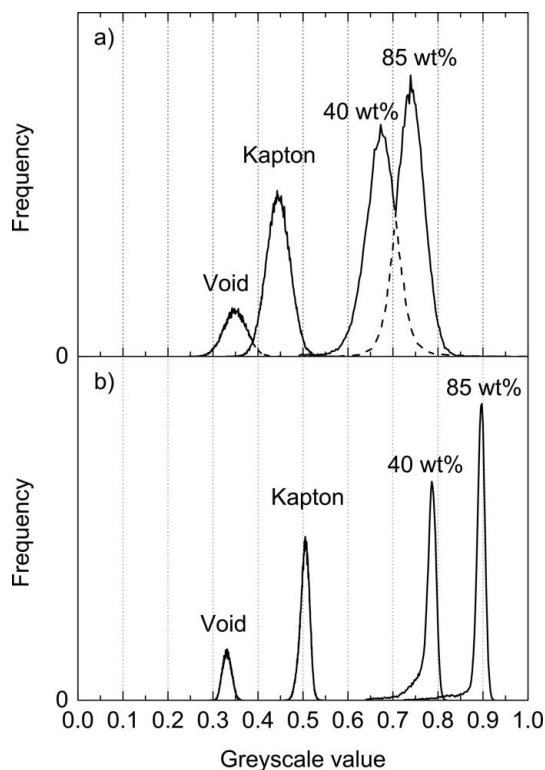


**Figure 2**  
Comparison of absorption (a) and phase (b) contrast of XTM imaging (20 keV, 2001 projections) of 40% and 85% H<sub>3</sub>PO<sub>4</sub> in a kapton sample holder.

the analysis significantly less complex. It should be noted, however, that the reduced noise contributions of phase-contrast-based reconstructions are concomitant with a reduced spatial resolution. If not otherwise specified, all subsequent images have been obtained exploiting phase contrast using the parameters given in Table 1.

### 3.2. Complete HT-PEFC MEA

In this section the complete MEA system is introduced by means of an image recorded *ex situ*, and a methodology is presented to retrieve the PA volume in the GDL.

A vertical slice through a MEA, illustrating the different layers, is given in Fig. 3. The sandwich-like geometry becomes clearly visible, with membrane and CLs in between the PA-

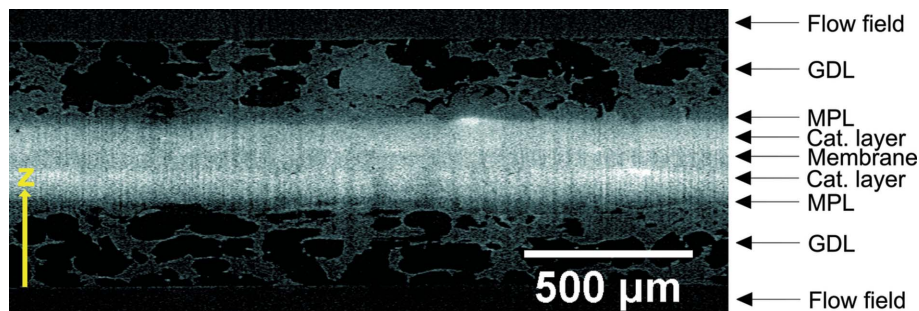


**Figure 3**  
Detail of a vertical slice through the MEA with an indication of the individual phases and the z-coordinate.

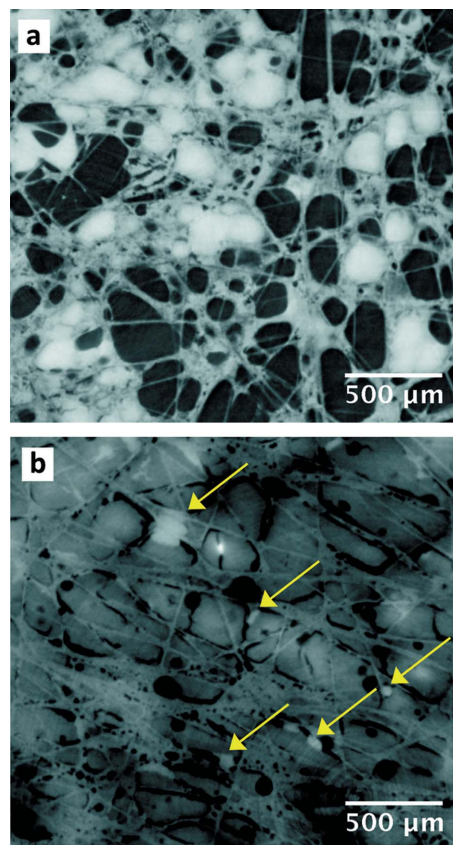


**Figure 4**  
Horizontal slices of (a) GDL and (b) MPL imaged using phase contrast at 20 keV; yellow arrows indicate PA-filled cracks and voids in MPL.

wetted carbon fibres of the GDL. In this perspective the MPL is masked by the highly attenuating Pt of the CL and the PA within the MPL micropores.

In Fig. 4(a), horizontal slices through the GDL and MPL are shown. In the GDL (Fig. 4a) the PA-filled macropores are clearly visible as well as carbon fibres and the carbonaceous binder, both wetted with PA. In Fig. 4(b), cracks and voids in the MPL are visible, which are partially filled with PA (yellow arrows) and act as a main path for PA from the membrane into the GDL and the flow field. In both images, PA and PA-wetted fibres have a high greyscale value and the void a low greyscale value, while the carbonaceous MPL and non-wetted fibres in Fig. 4(b) have an intermediate greyscale value.

Fig. 5 shows a horizontal slice of the GDL after washing out all PA. This tomogram was recorded in absorption mode in order to include the high-frequency components for better segmentation accuracy. When comparing with Fig. 4, the higher noise level is clearly visible. Qualitative comparison of the GDL slice in Fig. 4(a) with the dry slice in Fig. 5 shows that in the PA-wetted GDL almost no greyscale difference between the binder and

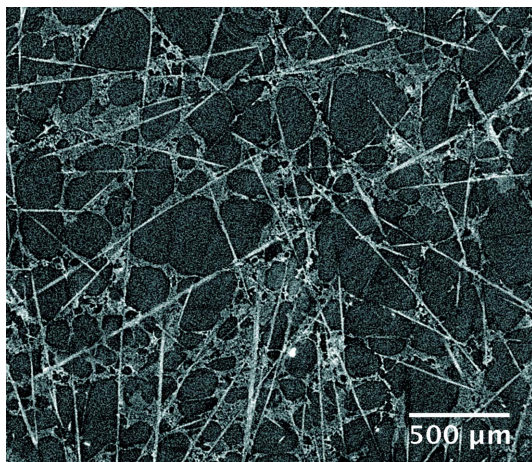


**Figure 5**  
Horizontal slice of PA-free GDL with carbon fibres (white) and binder (light grey). Imaged exploiting absorption contrast at 20 keV.

carbon fibres is observed but that a significant difference between the two carbonaceous components is present in the dry GDL. This indicates that the strongly absorbing PA is present within the micropores of the carbonaceous binder.

The porosity of PA-free and PA-wetted GDLs was determined by segmenting each horizontal slice in the images with a constant threshold into void/carbon and void/PA + carbon, respectively. Thereby the porosity of the GDL with and without PA was determined. The results are shown as a function of the GDL  $z$ -coordinate in Fig. 6. A  $z$ -dependence of the porosity is observed which is attributed to varying amounts of binder with the GDL thickness. The sample is compressed by 7%. With this compression the dry GDL exhibits a porosity of 74% close to the flow field with a decrease to a minimum of 63%. Close to the MPL a maximum of 82% is reached. The strong decrease in porosity at 110  $\mu\text{m}$  is due to protruding of the MPL. The average porosity is 71% for the dry sample. Since no data sheet values for the sample porosity are available, a quantitative comparison cannot be performed but previous work by Flückiger (2009) showed

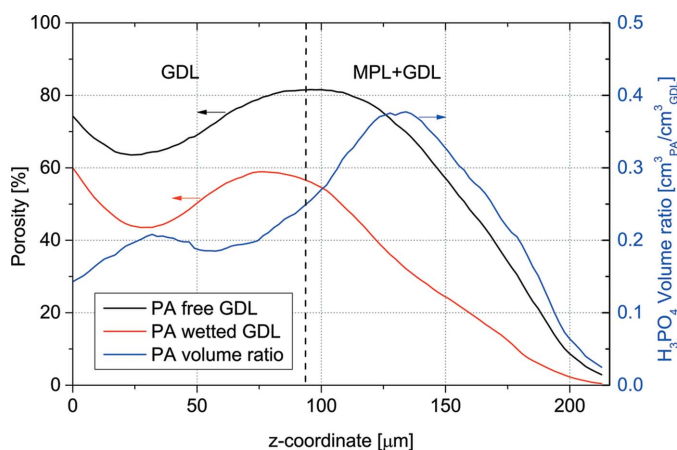


**Figure 6**  
Porosity of the GDL with and without  $\text{H}_3\text{PO}_4$  and calculated volume ratio (PA volume/GDL volume).

good agreement of XTM-determined porosities with mercury intrusion and decane wetting porosimetry. It should be noted that the determined values do not include the micropores of the binder which are not accessible with the given voxel size of 2.2  $\mu\text{m}$ . The PA-wetted sample exhibits a similar porosity characteristic as the dry sample with a maximum PA volume close to the MPL/CL.

### 3.3. Gas diffusion layer

The GDL is composed of carbon fibres forming macropores for gas transport and carbonaceous binder with a microporous structure. PA can accumulate in both macro- and micropores, but only PA in the macropores can be directly determined by segmentation due to the pixel size of 2.14  $\mu\text{m}$ . Therefore, the formation of three peaks, *i.e.* void, PA + C and PA, is expected in the histogram of the GDL. On the right-hand side of Fig. 7, details of the PA-wetted GDL are shown for 40, 60, 85 and 100 wt%  $\text{H}_3\text{PO}_4$  with the respective histograms on the left. In the case of 40 wt%  $\text{H}_3\text{PO}_4$ , due to similar electron density of the acid, the PA and the PA + C peaks fall together, as seen in the histogram. With higher concentrations, the PA peak becomes clearly visible and the peak maximum detectable. By applying a Gaussian fit to the PA + C and PA peaks for the three different concentrations, the noise contributions are reduced. The resulting greyscale peak values are plotted in Fig. 8 and a linear relation for the pure PA in the macropores is determined,

$$c(\text{PA}) [\text{wt}\%] = 205 \text{ gsv} - 5 \quad (R^2 = 0.998). \quad (1)$$

A linear concentration to greyscale dependency can also be observed for the binary PA + C mixture,

$$c(\text{PA}_{\text{GDL}}) [\text{wt}\%] = 248 \text{ gsv} - 13 \quad (R^2 = 0.984), \quad (2)$$

where  $c$  is the PA concentration in wt% and gsv the greyscale value of the PA and PA + C phases. With these relations the PA concentrations can be determined for samples with unknown state of the PA for the binary carbon and acid mixture as well as the pure PA in macropores.

It should be noted that the presented calibration has certain constraints. First, the PA + C calibration is influenced by the filling degree of the micropores. For this calibration experiment the pores are expected to be fully filled with PA. If the pore-filling degree is different from that in the calibration reference, then the binary PA + C phase becomes a ternary PA + C + void phase, which has a lower electron density and consequently the peak shifts towards lower greyscale values. This would result in deviation of the determined concentration, with lower concentrations calculated than actually present in the sample. When this methodology is applied for *in operando* PA concentration determination, it is therefore recommended to track the pure PA peak, which is independent of the amount of PA in the micropores of the binder. Second, the smallest errors are expected for high PA concentrations where the PA + C and PA peaks can clearly be distinguished and an accurate Gaussian peak fit can be performed.

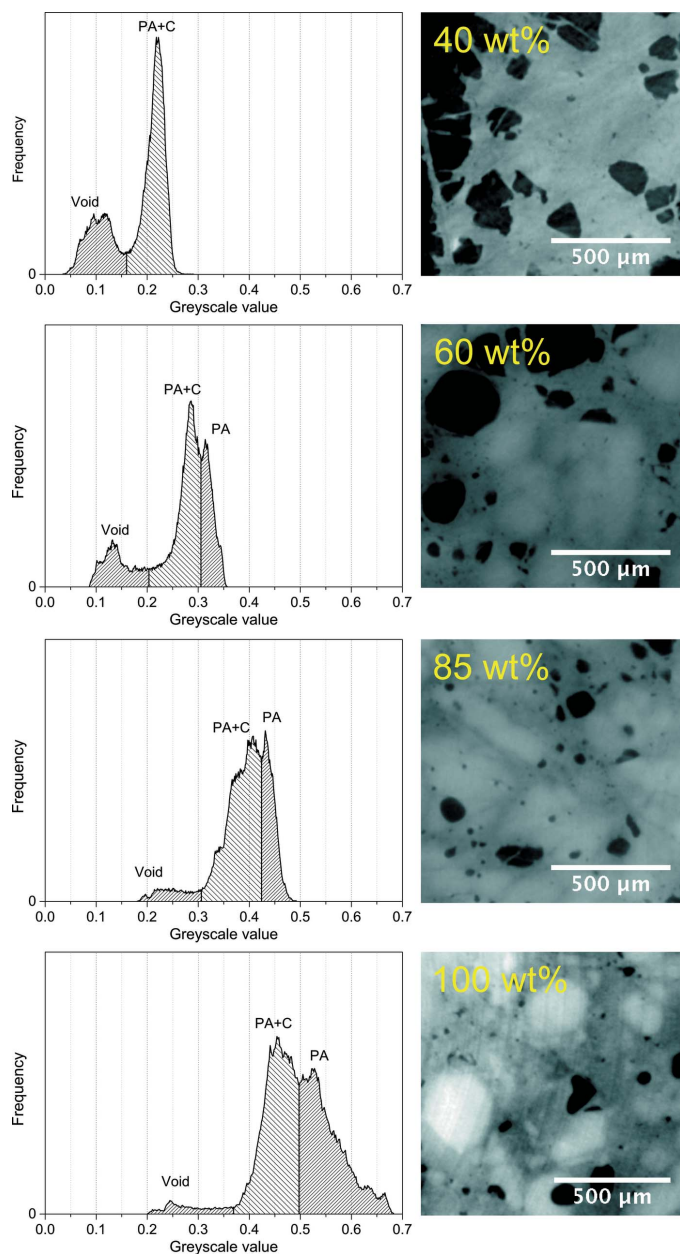


**Figure 7** Left row: horizontal slices of GDL impregnated with PA of 40, 60, 85 and 100 wt% (top to bottom); right row: corresponding histograms of the image sections in the left row; imaged in phase contrast mode at 20 keV.

The density to concentration relation of PA is well known (Christensen & Reed, 1955; MacDonald & Boyack, 1969), and hence determination of the mass of PA in the GDL becomes possible. For high PA concentrations this is done by segmenting the pure PA in the GDL. For low PA concentrations the two phases PA and PA + C cannot be separated. The mass of PA is then determined by subtraction of the slice-dependent carbon volume obtained from a dry sample as depicted in Fig. 6. In both cases the information of PA volume within the binder micropores is lost and might lead to significant underestimation of PA within the GDL structure. In low-temperature PEFC, water in the GDL is determined by direct

**Table 2** Comparison of the determined  $H_3PO_4$  mass by ion-chromatography (IC) and XTM.

Method	Sample thickness ( $\mu\text{m}$ )	$H_3PO_4$ concentration (wt%)	$H_3PO_4$ density ( $\mu\text{g cm}^{-3}_{\text{GDL}}$ )
XTM	214	52	15.93
IC	261	$52 \pm 2.6\%$	$15.41 \pm 0.80$

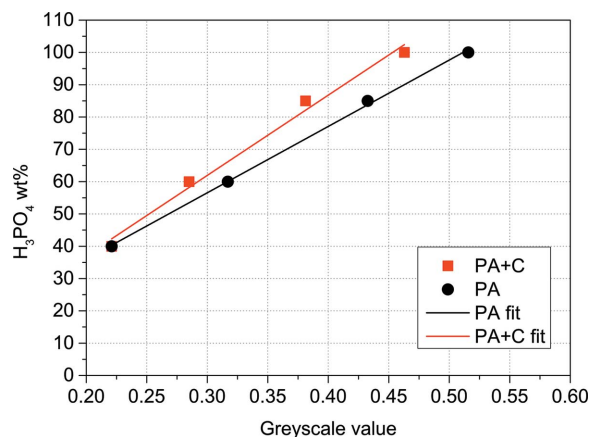


**Figure 8** Calibration results for the pure PA and the PA + C binary mixture in the GDL including a linear fit.

image subtraction of the dry structure from the wetted sample (Sinha *et al.*, 2006; Hartnig *et al.*, 2008; Eller *et al.*, 2011). A similar procedure was also considered (by removing PA from the sample in this case). However, it was deemed not to be feasible due to the extensive shrinkage of the membrane and consequent movement and deformation of the GDL after acid removal.

In order to check the quality of the calibration results in Fig. 8, the methodology was tested with a pristine MEA, where the mass of PA in the GDL determined by XTM is compared with the mass of PA obtained from washing out and chemical analysis of the resulting solution with ion chromatography (Table 2). The analysis of the XTM data is performed as previously described in this section using the PA + C segmentation approach to retrieve the PA volume and consequently the mass by comparing the PA greyscale value with the calibration data.

The results for the acid concentration and density (mass of PA per volume GDL) match well for both methods. It should be noted that the sample volume for ion-chromatography measurements was slightly larger due to MPL fragments still attached to the GDL and the 7% compression of the XTM sample upon cell assembly. Conclusively it can be stated that the mass and concentration determination by XTM is closely in line with the chemical analysis.

### 3.4. Catalyst layer

For the CL, segmentation of the PA phase, and hence quantification, is not possible due to pore size, which is considerably smaller than the voxel size of 2.14  $\mu\text{m}$ .

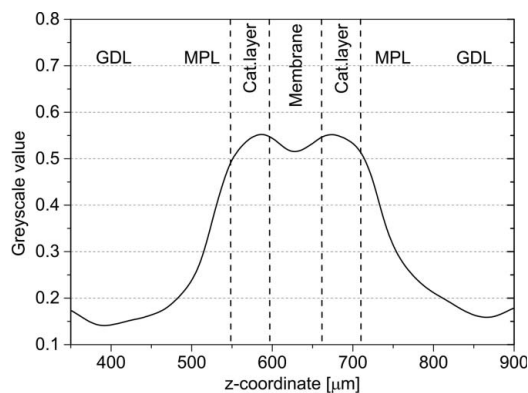


**Figure 9**  
Mean greyscale values of horizontal slices of MEA as a function of the  $z$ -coordinate in the catalyst layer for a sample equilibrated with 40 wt%  $\text{H}_3\text{PO}_4$ .

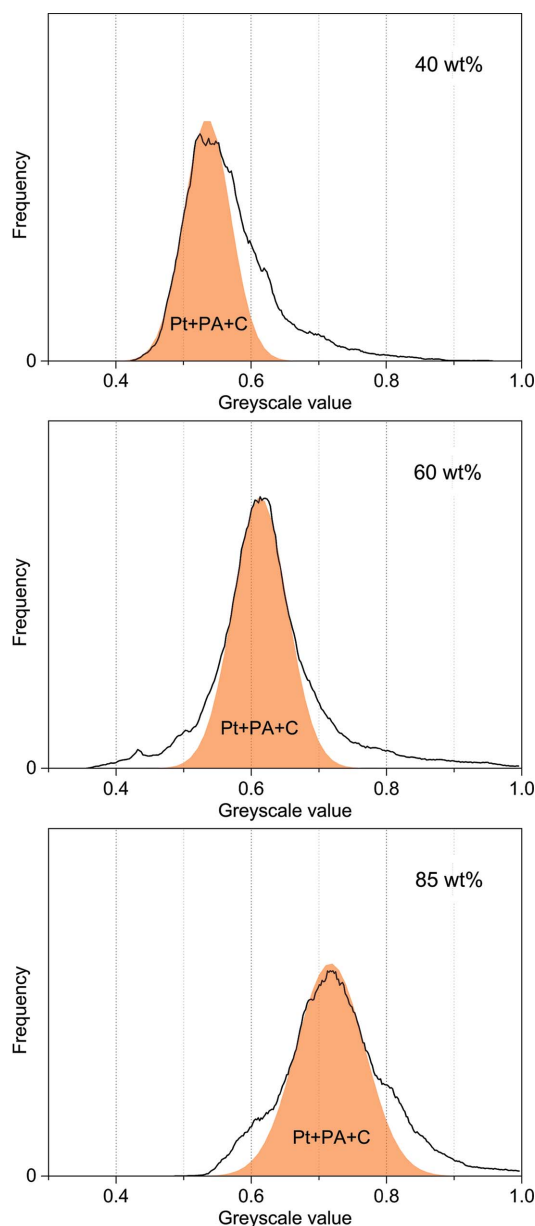


**Figure 10**  
Histograms of the slice with the maximum average greyscale value in the catalyst layer for samples equilibrated with 40, 60 and 85 wt% PA.

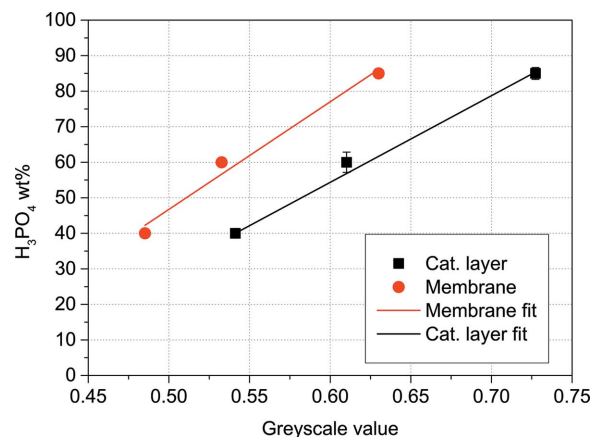


**Figure 11**  
Calibration curve for the catalyst layer and membrane including a linear fit.

However, changes in electron density in the CL can still be analyzed and information on concentration of PA obtained. The histogram of a horizontal slice in the CL yields the average electron density of the complex carbon black, platinum and PA mixture. The analysis for the CL is therefore performed as follows. First, the mean greyscale value for each horizontal slice in the MEA is calculated as illustrated in Fig. 9. The peak maxima correspond to the maximum Pt-to-PA ratio of the anode and cathode CLs. Second the histogram of this slice is analyzed as illustrated in Fig. 10, where the ternary mixtures of Pt + PA + C are shown. The tail of the peak at high greyscale values can be attributed to Pt-agglomerates, clearly visible as bright white spots in the horizontal slices (*cf.* Fig. 3). To reduce the influence of noise, a Gaussian fit is used to find the maximum greyscale value of the ternary mixture. Slightly different values for the anode and cathode CL are found, possibly due to noise contributions and platinum loading variations. Therefore the arithmetic mean between the two CLs was used and indicated by the error bars in Fig. 11.

The final calibration curve for the CL is shown in Fig. 11. The calibration curve can be described by the following equation,

$$c(\text{PA}_{\text{catalyst layer}}) [\text{wt}\%] = 243.87 \text{ gsv} - 91.98 \quad (R^2 = 0.997), \quad (3)$$

where  $c$  is the concentration in wt% and gsv the greyscale value of the Pt + PA + C peak.

### 3.5. Membrane

The membrane is a binary mixture of PBI and PA. It acts as the main PA source for the fuel cell, and hence the nanopores of the polymer matrix in the membrane can be considered to be always completely filled, independent of the PA concentration. Therefore, a volume change will not influence the calibration results. In Fig. 11 the concentration to greyscale value dependency is plotted for the membrane. It is described by the following equation,

$$c(\text{PA}_{\text{membrane}}) [\text{wt}\%] = 302.77 \text{ gsv} - 104.64 \quad (R^2 = 0.965). \quad (4)$$

The results were retrieved in analogy with the procedure for the catalyst layer, where the histogram of the slice in the membrane with the minimum mean greyscale is calculated and the peak position determined by a Gaussian fit.

### 3.6. Influence of temperature

When this calibration procedure is to be used for the determination of the PA concentration of *in operando* HT-PEFCs, the temperature influence of the recorded calibration data has to be taken into account. With increasing temperature, a decrease in PA density will lead to a decrease in the greyscale value of PA. Since the correlation of greyscale values to temperature is unknown for the used in-line phase contrast method, the calibration data will need to be recorded at the same temperature as the final *in operando* experiment.

## 4. Conclusions

Synchrotron-based X-ray tomographic microscopy is used to determine the distribution and concentration of phosphoric acid in the membrane electrode assembly of high-temperature polymer electrolyte fuel cells. The described methodology is applied at room temperature under non-operating conditions. For determination of the PA distribution in the macroporous gas-diffusion layer, absorption and phase contrast imaging can be used. However, for PA concentration determination it is shown that propagation-based phase contrast is superior to absorption contrast due to higher contrast and less noise. The formation of mixed phases of PA and the fuel cell components, e.g. micro- and macroporous gas diffusion layer, catalyst layer and membrane, makes the analysis of the tomograms challenging with respect to PA quantification. Therefore, a calibration method was developed to establish correlations between greyscale values and PA concentrations in the intermixed phases. The presented method thus allows PA concentration to be determined and the H<sub>3</sub>PO<sub>4</sub> mass in the GDL to be quantified. The comparison of ion-chromatography measurements with XTM indicates reasonable accuracy of the obtained data. In the catalyst layer and membrane the calibration allows for the determination of the PA concentration. In contrast to X-ray radiography the additional three-dimensional information of the tomography experiments allows for direct quantification of PA. Knowledge about simultaneous changes in volume and concentration of PA significantly simplify the analysis and allow for quantification in the GDL.

When the described methodology using phase contrast is to be applied for PA concentration determination of *in operando* HT-PEFCs, a repetition of the calibration at the operating temperatures is required because the PA density is temperature-dependent. Future work will extend the determination of PA distribution and possibly of PA concentration to *in operando* HT-PEFCs.

Financial support by BASF SE, precise machining work by M. Hottiger, software and electronic support by T. Gloor and the support at the TOMCAT beamline by J. Roth, J. Eller and M. Toulec are gratefully acknowledged.

## References

- Boillat, P., Biesdorf, J., Oberholzer, P., Kaestner, A. & Schmidt, T. J. (2014). *J. Electrochem. Soc.* **161**, F192–F198.
- Brown, E. H. & Whitt, C. D. (1952). *Ind. Eng. Chem.* **44**, 615–618.
- Chin, D. & Chang, H. H. (1989). *J. Appl. Electrochem.* **19**, 95–99.
- Christensen, J. H. & Reed, R. B. (1955). *Ind. Eng. Chem.* **47**, 1277–1280.
- Eller, J., Rosén, T., Marone, F., Stampanoni, M., Wokaun, A. & Büchi, F. N. (2011). *J. Electrochem. Soc.* **158**, B963–B970.
- Flückiger, R. (2009). *Transport Phenomena on the Channel-Rip Scale of Polymer Electrolyte Fuel Cells*, Dissertation, ETH Zürich, No. 18509.
- Flückiger, R., Marone, F., Stampanoni, M., Wokaun, A. & Büchi, F. N. (2011). *Electrochim. Acta*, **56**, 2254–2262.
- Hartnig, C., Manke, I., Kuhn, R., Kardjilov, N., Banhart, J. & Lehnert, W. (2008). *Appl. Phys. Lett.* **92**, 134106.
- Hartnig, C. & Schmidt, T. J. (2011). *Electrochim. Acta*, **56**, 4237–4242.
- Korte, C. (2012). *Fuel Cell Science and Engineering: Materials, Processes, Systems and Technology*, edited by D. Stolten and B. Emonts, pp. 335–359. Weinheim: Wiley-VCH.
- Krüger, P., Markötter, H., Haussssssmann, J., Klages, M., Arlt, T., Banhart, J., Hartnig, C., Manke, I. & Scholta, J. (2011). *J. Power Sources*, **196**, 5250–5255.
- Kuhn, R., Scholta, J., Krüger, P., Hartnig, C., Lehnert, W., Arlt, T. & Manke, I. (2011). *J. Power Sources*, **196**, 5231–5239.
- MacDonald, D. I. & Boyack, J. R. (1969). *J. Chem. Eng. Data*, **14**, 380–384.
- Maier, W., Arlt, T., Wannek, C., Manke, I., Riesemeier, H., Krüger, P., Scholta, J., Lehnert, W., Banhart, J. & Stolten, D. (2010). *Electrochem. Commun.* **12**, 1436–1438.
- Maier, W., Arlt, T., Wippermann, K., Wannek, C., Manke, I., Lehnert, W. & Stolten, D. (2012). *J. Electrochem. Soc.* **159**, F398–F404.
- Makharia, R., Mathias, M. F. & Baker, D. R. (2005). *J. Electrochem. Soc.* **152**, A970–A977.
- Marone, F. & Stampanoni, M. (2012). *J. Synchrotron Rad.* **19**, 1029–1037.
- Paganin, D., Mayo, S. C., Gureyev, T. E., Miller, P. R. & Wilkins, S. W. (2002). *J. Microsc.* **206**, 33–40.
- Pahari, S., Choudhury, C. K., Pandey, P. R., More, M., Venkatnathan, A. & Roy, S. (2012). *J. Phys. Chem. B*, **116**, 7357–7366.
- Roth, J., Eller, J., Marone, F. & Büchi, F. N. (2013). *J. Phys. Chem. C*, **117**, 25991–25999.
- Schmidt, T. J. & Baumeister, J. (2006). *ECS Trans.* **3**, 861–869.
- Seel, D. C., Benicewicz, B. C., Xiao, L. & Schmidt, T. J. (2010). *Handbook of Fuel Cells*, edited by W. Vielstich, A. Lamm, H. A. Gasteiger and H. Yokokawa, pp. 1–13. New York: John Wiley and Sons.
- Sinha, P. K., Halleck, P. & Wang, C. Y. (2006). *Electrochem. Solid State Lett.* **9**, A344–A348.
- Stampanoni, M., Groso, A., Isenegger, A., Mikuljan, G., Chen, Q., Bertrand, A., Henein, S., Betemps, R., Frommherz, U., Böhler, P., Meister, D., Lange, M. & Abela, R. (2006). *Proc. SPIE*, **6318**, 63180M.
- Wannek, C., Konradi, I., Mergel, J. & Lehnert, W. (2009). *Int. J. Hydrog. Energy*, **34**, 9479–9485.
- Wydeven, T. (1959). *J. Chem. Eng. Data*, **11**, 174–176.
- Yu, S., Xiao, L. & Benicewicz, B. C. (2008). *Fuel Cells*, **8**, 165–174.